Optimal heat transport induced by magnetic nanoparticle delivery in vascularised tumours

Tahani Al Sariri [a,b], Radostin D. Simitev [a], Raimondo Penta [a,*]

[a] *School of Mathematics and Statistics, University of Glasgow, University Place, Glasgow, G12 8QQ, UK*
[b] *Department of Mathematics, College of Science, Sultan Qaboos University, Al-Khoudh 123, Oman*

A B S T R A C T

We describe a novel mathematical model for blood flow, delivery of nanoparticles, and heat transport in vascularised tumour tissue. The model, which is derived via the asymptotic homogenisation technique, provides a link between the macroscale behaviour of the system and its underlying, tortuous micro-structure, as parametrised in Penta and Ambrosi (2015). It consists of a double Darcy's law, coupled with a double advection–diffusion–reaction system describing heat transport, and an advection–diffusion–reaction equation for transport and adhesion of particles. Particles are assumed sufficiently large and do not extravasate to the tumour interstitial space but blood and heat can be exchanged between the two compartments. Numerical simulations of the model are performed using a finite element method to investigate cancer hyperthermia induced by the application of magnetic field applied to injected iron oxide nanoparticles. Since tumour microvasculature is more tortuous than that of healthy tissue and thus suboptimal in terms of fluid and drug transport, we study the influence of the vessels' geometry on tumour temperature. Effective and safe hyperthermia treatment requires tumour temperature within certain target range, generally estimated between 42 °C and 46 °C, for a certain target duration, typically 0.5h to 2h. As temperature is difficult to measure in situ, we use our model to determine the ranges of tortuosity of the microvessels, magnetic intensity, injection time, wall shear stress rate, and concentration of nanoparticles required to achieve given target conditions.

1. Introduction

Hyperthermia therapy (HT) is an emerging anti-cancer treatment in which a tumour is exposed to abnormally high temperature causing damage or necrosis of cancer tissue. Hyperthermia induced cell necrosis is mostly a result of conformational changes leading to destabilisation of macromolecule structures and disruptions in cell metabolism, inhibition of DNA repair, and initiation of cellular apoptotic pathways (Oei et al., 2015). In addition to its direct anti-tumour effects, HT enhances the anti-cancer effects of radiotherapy and chemotherapy. A hyperthermia treatment can be applied locally or over the whole body depending on the type of tumour, its size and location (Kok et al., 2020; Cherukuri et al., 2010; Chicheł et al., 2007). Magnetic nanoparticles are increasingly being used for this purpose as they can produce a heat source localised in the tumour region without significantly affecting the surrounding healthy tissue, e.g. Colombo et al. (2012) and Das et al. (2019). Nanoparticles are typically introduced to the tumour either directly or via the blood stream. The patient is then exposed to an alternating magnetic field leading to heat generation due to magnetic hysteresis effects. In addition to heating tissues, nanoparticles can be used also for localised drug delivery (Laurent et al., 2011).

The main clinical determinants of the efficacy of hyperthermia in destroying cancer cells are (a) the temperature achieved within the tissue above normal body temperature and (b) the duration of time for which this abnormal temperature is maintained. In the article we refer to these as "hyperthermic temperature" and "hyperthermic duration" and they are also commonly known as hyperthermia "thermometric parameters". For the treatment to be effective but safe both the hyperthermic temperature and the hyperthermic duration must be kept withing certain target ranges (Kok et al., 2020; Ademaj et al., 2022). The hyperthermic temperature and duration depend on the properties of the nanoparticles employed, (e.g. shape, density, magnetisation), the properties of the externally applied magnetic field (frequency and intensity) and the properties of the tumour tissue as these affect blood perfusion (vascularisation, tortuosity) as discussed by Shubitidze et al.

(2015) and Golneshan and Lahonian (2011). Direct in situ measurements of hyperthermic temperature and duration are usually impossible and it is the main goal of this work to estimate the values of these important clinical measures using a newly-developed mathematical model of a vascularised tumour.

There is large uncertainty and variability in the estimates of safe and effective thermometric parameter values and ranges reported in the literature. One clinical study reports that hyperthermic temperature must be greater that 41 °C and must be maintained for a hyperthermic duration of over 60 min (Ademaj et al., 2022). Another study finds that approximately 90% of the cells can be eradicated with hyperthermic temperature greater than 43 °C (Bhuyan et al., 1977). However, an hyperthermic temperature which is larger than 43.5 °C or 44 °C, is found to increase the general levels of cytotoxicity in the body (Overgaard et al., 1991). Furthermore, a temperature increase can induce thermotolerance in cancer cells, meaning that an increase in the hyperthermic duration for cells who have already undergone a hyperthermia treatment may be required to achieve the same results in terms of necrosis (Law, 1979). In general, the thermometric parameters cannot be expected to have single fixed values, rather the effects of a hyperthermia treatment likely vary on a spectrum (Bing et al., 2019).

Even when target values of the hyperthermic temperature and duration are known with sufficient accuracy, it remains a non-trivial task to fine-tune the parameters of a hyperthermia treatment procedure so that these thermometric targets are achieved. It is usually very difficult to measure temperature in situ within a tumour tissue non-invasively and even more so while treatment is underway and as a consequence a variety of experimental and theoretical investigations have been reported in the literature. Muela et al. (2016) suggest optimal parameters for hyperthermia treatment by estimating the specific absorption rate (SAR) of biomineralized magnetite nanoparticles by simulation of the dynamic hysteresis loops from the Landau–Liftshitz–Gilbert equation which are then compared to experimental measurements in water and agarose gel. Roohi et al. (2021, 2020) estimate the optimal location, dosage, duration time of injecting magnetic nanoparticles employing a dual phase lag bioheat equation in conjunction with a mass transfer model for magnetic particles and proceed by optimising the protocol using a simulated annealing algorithm. Tang (2018) use machine learning procedures and heuristic algorithms to predict magnetic nanoparticle infusion in tumour tissue and then estimate the temperature field. Further attempts in this direction are reported by Lang et al. (1999), Saeedi et al. (2017) and Cervadoro et al. (2013) to mention few ones.

The main advantage of our work lies in the development and use of a cutting-edge multiscale mathematical model of a vascularised tumour. Both the hyperthermic temperature and duration are influenced by the properties of the injected nanoparticles (e.g. the diameter of the particles and their shape), injection conditions, and, especially for vascularised tumours, by the structural and functional characteristics of the microvessels, such as their geometrical arrangement and wall shear rate. In particular, the geometrical properties of the tumour vascularisation are well-known to significantly affect blood and drug transport in cancer (Jain and Baxter, 1988; Jain et al., 2007). The role of the microvessels' geometry has been further elucidated and quantified by means of suitable homogenisation approaches, which are capable of providing a link between the *micro*-scale, where the distance between individual vessels can be clearly identified, and the *macro*-scale of the tissues, where experimental measurements are usually performed. Penta and Ambrosi (2015) and Mascheroni and Penta (2017) quantified the role of microvascular tortuosity on fluid and macromolecules transport in cancerous tissues, respectively, based on the theoretical results derived via asymptotic homogenisation in Shipley and Chapman (2010) and Penta et al. (2015). They showed that geometrical complexity can dramatically impair blood and drug perfusion within the tumour mass and may limit the efficacy of transport-based anti-cancer therapies in that drug cannot adequately reach the innermost tumorous regions. In Al Sariri and Penta (2022), the authors

generalised the mathematical model illustrated in Penta et al. (2015) to address heat transport driven by small nanoparticles in both the interstitial tumour space and the microvessels in the context of cancer hyperthermia. They obtained a new system of macroscale PDEs of double Darcy's, double advection–diffusion–reaction type which takes into account fluid, nanoparticles, and heat transport in the tumour. Blood, heat and also nanoparticles exchange is also taken into account, as the nanoparticles are assumed sufficiently small in order for their extravasation through the vessels' walls to occur. The authors show that microvessels' tortuosity impaires heat transport in vascular tumours, and that regularisation of the microvessels' network can result in a significant increase in temperature (1–2 °C).

In this work, we extend the analysis carried out by Al Sariri and Penta (2022), which concerns individual nanoparticles characterised by a very small diameter which can extravasate from the vessels to the tumour to large nanoparticles, which can be manufactured in the form of vascular magnetic nanoconstructs, as illustrated for example by Gizzatov et al. (2014) and Nabil and Zunino (2016) (see Fig. 1). We start from a new homogenised model which is derived by taking into account that in this latter case nanoparticles cannot extravasate from the vessels into the tumour interstitium. As such, the nanoparticle dynamics is present in the vessels only and we explicitly take into account the role of particles adhesion.

The specific absorption rate that determines heat generation under applied magnetic field is computed using a Brownian and Neels relaxation formula. The model allows to estimate the spatiotemporal distribution of temperature within the tumour tissue and we use this to make accurate estimates of the hyperthermic temperature and duration as functions of the parameters that describe nanoparticle properties (magnetic material, size), microvasculature properties (tortuosity, hydraulic conductivity, thermal conductivity, adhesion rate) and the properties of applied magnetic field (intensity and frequency). The work is organised as follows. In Section 2, we describe the new homogenised model which describes the interplay between fluid, nanoparticles, and heat transport in a vascularised tumour subjected to the action of an applied magnetic field. The role of nanoparticles adhesion and a comparison between this work and Al Sariri and Penta (2022) is highlighted. In Section 3, we discuss the results. In 3.1 we focus on both temporal and spatial temperature and nanoparticles' concentration maps at varying tortuosity and for different nanoparticles' material in Section. In Section 3.2 we discuss the optimal heat transport parameters to achieve physiologically safe hyperthermic temperature and duration. Finally, we discuss limitations of the model and further perspectives in Section 4.

2. Mathematical modelling

The velocity of nanoparticles in the vessels is in general heterogeneous. The particles which are closer to the walls of the vessels are slower than the others. This is due to the friction force between the particles and the vessel membrane in a process which is known as *adhesion*. The typical *extravasation* transport mechanism consists of nanoparticles being transported into the tumour interstitium through the pores of the vessels (these are for example of the order of 40–200 nm diameter for brain and peripheral tumour according to the analysis performed by Sarin et al. (2009) by means of electronic microscopy techniques). However, transport of nanoparticles depends on the ratio between particle size and vessel wall pore size (Stylianopoulos et al., 2018). Nanoparticles with diameter less than 10 nm can be easily filtered by the renal system and they can be captured by spleen and liver if their size is greater than 200 nm. The optimal nanoparticle diameter is therefore usually estimated to range from 20 to 200 nm, as discussed by Thomas et al. (2013). Here we study transport of large (80 nm in diameter) spherical magnetic nanoparticles in three-dimensional vascularised tumours. As such, we assume that nanoparticles adhere to vessel walls and extravasation is ruled out. The tumour, which is
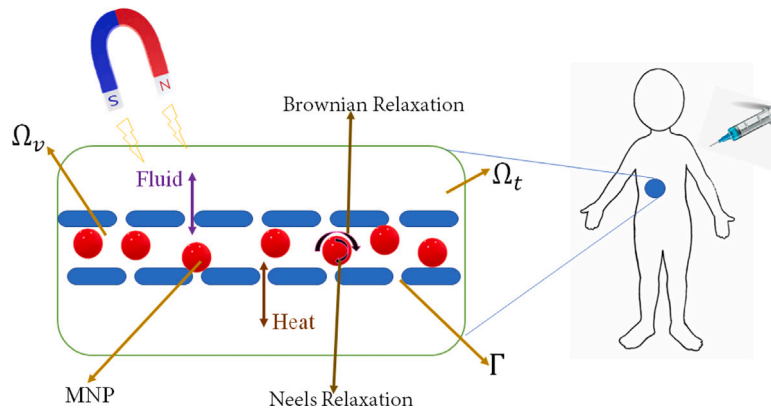
Fig. 1. A schematic diagram of hyperthermia cancer treatment using large size of magnetic nanoparticles (MNP).

identified with a three-dimensional domain Ω, is assumed to comprise of two regions, namely, tumour vessels Ω_v and tumour interstitium Ω_t. Therefore, vessel walls play the role of the interface between these two compartments, which is here denoted by $\Gamma = \partial\Omega_v \cap \partial\Omega_t$. The system is intrinsically multiscale due to the sharp difference between the average intercapillary distance d and the size of the whole tumour tissue L, therefore motivating the development of a multiscale modelling approach. In particular, we define a small parameter ϵ which expresses these two characteristics lengths as

$$\epsilon = \frac{d}{L}. \tag{1}$$

Next we illustrate the mathematical modelling assumptions which we embrace as a starting point to describe transport of fluid, nanoparticles' delivery and convection–diffusion of heat in the context of cancer hyperthermia (see Fig. 1).

2.1. Fluid flow

We consider the blood as an incompressible viscous fluid modelled by the following Stokes' problem

$$\mu\nabla^2\mathbf{u}_v = \nabla p_v \quad \text{in} \quad \Omega_v, \tag{2a}$$

$$\nabla \cdot \mathbf{u}_v = 0 \quad \text{in} \quad \Omega_v, \tag{2b}$$

where $\mathbf{u}_v$ and p_v are the blood velocity and pressure in the capillaries, while μ is the blood viscosity.

We assume that the tumour interstitium is an isotropic porous medium, so that interstitial fluid flow can be described by Darcy's law

$$\mathbf{u}_t = -\kappa\nabla p_t \quad \text{in} \quad \Omega_t, \tag{3a}$$

$$\nabla \cdot \mathbf{u}_t = 0 \quad \text{in} \quad \Omega_t. \tag{3b}$$

Here, $\mathbf{u}_t$ and p_t are the fluid velocity and pressure in the tumour interstitium, and κ is the tissue conductivity.

The fluid is supplied continuously through the vessels' membrane and the flow relies on the pressure differences between the two regions, so that the flux continuity condition across the interface Γ reads

$$\mathbf{u}_t \cdot \mathbf{n} = \mathbf{u}_v \cdot \mathbf{n} = L_p(p_v - p_t) \quad \text{on} \quad \Gamma. \tag{4}$$

The above relationship is also known as *Starling's law* in the biophysical literature, and in general states that the fluid flux is proportional to the difference between the interstitial and vascular pressure, as well as the difference between the oncotic pressures in those compartments. However, following Penta et al. (2015), we are here neglecting the oncotic pressure contribution by considering that this pressure jump is often negligible for most tumour types, as reported for example in Jain et al. (2007). We specify the tangential components of the fluid flowing

in the vessels by means of a Beavers and Joseph condition which accounts for the slip over a porous surface as discussed for example by (Shipley and Chapman, 2010; Penta et al., 2015)

$$\mathbf{u}_v \cdot \tau_v = -\frac{\sqrt{\kappa}}{\varphi}[(\mathbf{n} \cdot \nabla)\mathbf{u}_v] \cdot \tau_v \quad \text{on} \quad \Gamma, \tag{5}$$

where L_p is the permeability of membrane, τ_v collectively denotes both of the unit vector tangent to the vessels' wall, φ is a non-dimensional parameter encoding structural properties of the membrane, and $\mathbf{n}$ is the unit outward vector normal to the vessels' wall.

2.2. Advection, diffusion, and adhesion of nanoparticles

The concentration of magnetic nanoparticles c_v which is delivered intravascularly is governed by the following advection–diffusion equation

$$\frac{\partial c_v}{\partial t} + \nabla \cdot (c_v\mathbf{u}_v - D_v\nabla c_v) = 0 \quad \text{in} \quad \Omega_v, \tag{6}$$

where the parameter D_v is the diffusivity of the particles. Mass transport in the vessels is affected by particles' size and shape (Hossain et al., 2013).

The adhesion between nanoparticles with different sizes and shapes and the vessels wall was discussed by Decuzzi and Ferrari (2006). The adhesion probability depends directly on the receptors and ligands densities, and the interaction area between the particle and the substrate. The Authors of the latter work found that oblate nanoparticles adhere to the vessels wall more than the spherical particles. Furthermore, the optimal size and shape for nanoparticles are influenced by the ratio between the density of the receptors and vessels' shear stress.

Here, we focus on spherical nanoparticles for the sake of simplicity and we assume that their size is greater than the vessels' pore size, so that we explicitly take into account the adhesion between the particles and vessels' wall. We model the latter mechanism by means of the following interface condition

$$(c_v\mathbf{u}_v - D_v\nabla c_v) \cdot \mathbf{n} = \Pi c_v \quad \text{on} \quad \Gamma. \tag{7}$$

Following the analysis carried out by Nabil and Zunino (2016), we assume that

$$\Pi = z|\xi|\frac{p_d}{2}, \tag{8}$$

where z is the adhesion probability, $|\xi|$ is the wall shear rate, and p_d is the diameter of the particle. The density of nanoparticles Ψ adhering to the vessels' wall is computed by

$$\frac{d\Psi}{dt} = \Pi c_v \quad \text{in} \quad \Omega_v. \tag{9}$$

2.3. Heat convection and diffusion

The heat generated within the tumour vessels and in the tumour interstitium is due to the magnetic field which is applied after injecting the nanoparticles. The field causes rotation and vibrations of the particles around themselves and around the field.

We use the Brownian and Neels relaxation formula to identify the absorption rate which is directly related to the heat distribution in the tumour tissue.

Heat transport in both the vessels and the tumour interstitial space is then described by a coupled system of heat convection–diffusion equations. We assume that there exists a volume heat source in the vessels which is proportional to both the concentration of nanoparticles c_v and the density of those adhering to the walls ψ, with proportionality constant given by the absorption rate α. In addition, we account for the heat exchanged between the vessels and the interstitial compartment. Finally, we also consider the influence of a given volume source in the interstitial space in order to fully capture the influence of the heat generated by the magnetic nanoparticles under the influence of an applied magnetic field. In this case, as the heat and (vascular) drug transport problems are decoupled, we assume that such a source is proportional to the absorption rate α and to a given function $\mathcal{R}$ which is in turn intended to be related to the average concentration of nanoparticles that are generating the heat which then plays a role in the whole tissue. The resulting governing equations can be written as

$$\gamma_t \rho_t \left[\frac{\partial T_t}{\partial t} + \nabla \cdot \left(T_t \mathbf{u}_t - \frac{K_t}{\gamma_t \rho_t} \nabla T_t \right) \right] = \alpha \mathcal{R} \quad \text{in } \Omega_t, \tag{10a}$$

$$\gamma_v \rho_v \left[\frac{\partial T_v}{\partial t} + \nabla \cdot \left(T_v \mathbf{u}_v - \frac{K_v}{\gamma_v \rho_v} \nabla T_v \right) \right] = \alpha \left(\psi + c_v \right) \text{ in } \Omega_v, \tag{10b}$$

where K_v, K_t, γ_v, γ_t, and ρ_v, ρ_t are the vessels and interstitial heat conductivities, specific heat capacities, and compartment densities, respectively. The parameter $\psi = \frac{\Psi}{L}$ has the dimensions of a concentration and represents an effective concentration of particles due to adhesion. The model can be derived for a generic given function $\mathcal{R}$, so that we shall specify its functional form when introducing the solution of the model.

We assume that heat can be exchanged between the tumour and the vessels, such that the heat flux across the membrane is proportional to the difference between the temperatures in the two compartments, as follows

$$\left(T_v \mathbf{u}_v - \frac{K_v}{\gamma_v \rho_v} \nabla T_v \right) \cdot \mathbf{n} = \frac{\beta}{\gamma_v \rho_v} \left(T_v - T_t \right) \quad \text{on } \Gamma, \tag{11a}$$

$$\left(T_t \mathbf{u}_t - \frac{K_t}{\gamma_t \rho_t} \nabla T_t \right) \cdot \mathbf{n} = \frac{\beta}{\gamma_t \rho_t} \left(T_t - T_v \right) \quad \text{on } \Gamma, \tag{11b}$$

where β is the heat transfer coefficient.

The heat generated by magnetic nanoparticles strongly depend on the absorption rate α, which depends on particles' size, shape, material, as well as magnetic field properties, i.e. intensity and frequency. According to Avolio et al. (2021), the parameter α is defined as

$$\alpha = \frac{\mu_0^2 \pi f H_0^2 M_d^2 V}{3 \rho_n K_B T} \frac{2\pi f \tau_{\text{eff}}}{1 + (2\pi f \tau_{\text{eff}})^2}, \tag{12}$$

where μ_0 is the magnetic permeability, M_d is the magnetisation of nanoparticles, K_B is Boltzmann's constant, T is the temperature, f is the field frequency, H_0 is the field intensity, V is the volume of nanoparticles, ρ_n is the density of nanoparticle, and τ_{eff} is the overall relaxation time which can be defined as

$$\frac{1}{\tau_{\text{eff}}} = \frac{1}{\tau_{\text{N}}} + \frac{1}{\tau_{\text{B}}}, \tag{13}$$

with

$$\tau_{\text{N}} = \tau_0 e^{\frac{k_i V}{K_B T}}, \quad \tau_{\text{B}} = \frac{3\eta V_H}{K_B T}. \tag{14}$$

Here, τ_0 is Larmor's time constant, k_i is the magnetic anisotropy constant, η is nanoparticles' carrier liquid viscosity, and V_H is the hydrodynamic volume which is computed by Torres et al. (2019) using

$$V_H = \pi \frac{(p_d + \delta)^3}{6}, \tag{15}$$

where $\delta = 2$ nm.

Remark (*Current model vs. Al Sariri and Penta, 2022*). Al Sariri and Penta (2022) discussed the hyperthermia cancer treatment using magnetic nanoparticles which can extravasate across the vessels' walls. Therein, the concentration of nanoparticles was then studied in both regions of the tumour tissue by means of advection–diffusion equations. The authors assumed that the particles could be uptaken by tumour interstitium after having been delivered intravascularly, such that

$$\frac{\partial c_v}{\partial t} + \nabla \cdot (c_v \mathbf{u}_v - D_v \nabla c_v) = 0 \quad \text{in } \Omega_v, \tag{16a}$$

$$\frac{\partial c_t}{\partial t} + \nabla \cdot (c_t \mathbf{u}_t - D_t \nabla c_t) = -\Lambda c_t \quad \text{in } \Omega_t, \tag{16b}$$

where the parameter Λ denoted the uptake rate in the tumour interstitium. In addition, they accounted for transvascular transport of nanoparticles via the following interface conditions

$$(c_v \mathbf{u}_v - D_v \nabla c_v) \cdot \mathbf{n} = (c_t \mathbf{u}_t - D_t \nabla c_t) \cdot \mathbf{n}$$
$$= L_c (c_v - c_t) \quad \text{on } \Gamma, \tag{17}$$

where L_c represents the diffusive permeability of the vessels' membranes. The differential equations governing heat transport in Al Sariri and Penta (2022) is analogous to that describe by the system (10a)–(10b) with interface conditions (11a)–(11b), however the absorption rate α was considered as a single, constant parameter, and its value was taken from Cervadoro et al. (2013). Also, the heat source of the system (10a)–(10b) did not depend on the density of adhering particles Ψ, as Al Sariri and Penta (2022) considered transport of small nanoparticles and therefore ignored nanoparticles' adhesion.

Next we perform a non-dimensional analysis of the model, which will then be upscaled by means of the asymptotic homogenisation technique.

2.4. Model non-dimensionalisation

We rewrite the system of Eqs. (2a)–(7), (9), and (10a)–(11b) in non-dimensional form by using the change of variables

$$c_v = C_r c_v', \ \mathcal{R} = C_r \mathcal{R}', \ \mathbf{u}_v = \frac{Cd^2}{\mu} \mathbf{u}_v', \ t = \frac{L\mu}{Cd^2} t', \ \nabla = \frac{1}{L} \nabla',$$
$$p = CLp', \ T = XT', \Psi = LC_r \Psi', \tag{18}$$

where C_r is the reference of concentration, C is pressure gradient, X is the reference temperature, d is the distance between capillaries, and L is the average size of the tumour. The corresponding non-dimensional system of PDEs, after having neglected the primes for the sake of simplicity of notation, can be written as

$$\mathbf{u}_t = -\bar{\kappa} \nabla p_t \quad \text{in } \Omega_t, \tag{19a}$$

$$\nabla \cdot \mathbf{u}_t = 0 \quad \text{in } \Omega_t, \tag{19b}$$

$$\epsilon^2 \nabla^2 \mathbf{u}_v = \nabla p_v \quad \text{in } \Omega_v, \tag{19c}$$

$$\nabla \cdot \mathbf{u}_v = 0 \quad \text{in } \Omega_v, \tag{19d}$$

$$\frac{\partial c_v}{\partial t} + \nabla \cdot (c_v \mathbf{u}_v - \bar{D}_v \nabla c_v) = 0 \quad \text{in } \Omega_v, \tag{19e}$$

$$\frac{d\Psi}{dt} = \bar{\Pi}_1 c_v \quad \text{in } \Omega_v, \tag{19f}$$

$$\left[\frac{\partial T_t}{\partial t} + \nabla \cdot (T_t \mathbf{u}_t - \bar{K}_t \nabla T_t) \right] = \bar{\alpha}_t \mathcal{R} \quad \text{in } \Omega_t, \tag{19g}$$

$$\left[\frac{\partial T_v}{\partial t} + \nabla \cdot (T_v \mathbf{u}_v - \bar{K}_v \nabla T_v) \right] = \bar{\alpha}_v (\psi + c_v) \text{ in } \Omega_v, \tag{19h}$$

with boundary conditions

$$\mathbf{u}_t \cdot \mathbf{n} = \mathbf{u}_v \cdot \mathbf{n} = \bar{L}_p(p_v - p_t) \quad \text{on} \quad \Gamma, \tag{20a}$$

$$\mathbf{u}_t \cdot \tau = -\epsilon \bar{\varphi}[(\mathbf{n} \cdot \nabla)\mathbf{u}_t] \cdot \tau \quad \text{on} \quad \Gamma, \tag{20b}$$

$$(c_v \mathbf{u}_v - \bar{D}_v \nabla c_v) \cdot \mathbf{n} = \epsilon \bar{\Pi} c_v \quad \text{on} \quad \Gamma, \tag{20c}$$

$$\left(T_v \mathbf{u}_v - \bar{K}_v \nabla T_v\right) \cdot \mathbf{n} = \epsilon \bar{\beta}_v \left(T_v - T_t\right) \quad \text{on} \quad \Gamma, \tag{20d}$$

$$\left(T_t \mathbf{u}_t - \bar{K}_t \nabla T_t\right) \cdot \mathbf{n}_t = \epsilon \bar{\beta}_t \left(T_t - T_v\right) \quad \text{on} \quad \Gamma. \tag{20e}$$

The non-dimensional numbers are defined as follows

$$\bar{\kappa} = \frac{\kappa \mu}{d^2}, \quad \bar{\Pi} = \frac{\Pi L}{Ud}, \quad \bar{\Pi}_1 = \frac{\Pi \mu}{Cd^2}, \quad \bar{L}_p = \frac{L_p L \mu}{d^2}, \quad \bar{\varphi} = \frac{\sqrt{\kappa}}{\varphi d}, \tag{21a}$$

$$\bar{\beta}_v = \frac{\beta L \mu}{Cd^3 \gamma_v \rho_v}, \quad \bar{\beta}_t = \frac{\beta L \mu}{Cd^3 \gamma_t \rho_t}, \tag{21b}$$

$$\bar{\alpha}_t = \frac{\alpha C_r L \mu}{XCd^2 \gamma_t \rho_t}, \quad \bar{\alpha}_v = \frac{\alpha C_r L \mu}{XCd^2 \gamma_v \rho_v}, \tag{21c}$$

while the non-dimensional diffusivities and heat conductivities for the vessels and tumour interstitium are given by

$$\bar{D} = \frac{D \mu}{LCd^2}, \quad \bar{K} = \frac{K \mu}{\rho \gamma LCd^2}. \tag{22}$$

2.5. The homogenised model

The homogenised model can be derived by applying the classical asymptotic (periodic) homogenisation technique, as discussed for example by Bakhvalov and Panasenko (1989), Papanicolau et al. (1978) and Hornung (1996), and many others, to our system. We first decouple spatial variations by introducing a microscale $\mathbf{y}$, which is related to the macroscale $\mathbf{x}$ by

$$\mathbf{y} = \frac{\mathbf{x}}{\epsilon}, \tag{23}$$

where ϵ now plays the role of an asymptotic parameter. We further assume that any variable q in the system is $\mathbf{y}$-periodic and can be written in power series of ϵ as follows

$$q(\mathbf{x}, t) = q(\mathbf{x}, \mathbf{y}, t) = \sum_{l=0}^{\infty} q^{(l)}(\mathbf{x}, \mathbf{y}, t)\epsilon^l =$$
$$q^{(0)}(\mathbf{x}, \mathbf{y}, t) + \epsilon q^{(1)}(\mathbf{x}, \mathbf{y}, t) + \epsilon^2 q^{(2)}(\mathbf{x}, \mathbf{y}, t) + \dots \tag{24}$$

The differential operators transform according to the chain rule as

$$\nabla \longrightarrow \nabla_x + \frac{1}{\epsilon} \nabla_y, \quad \nabla^2 \longrightarrow \nabla_x^2 + \frac{2}{\epsilon} \nabla_x \nabla_y + \frac{1}{\epsilon^2} \nabla_y^2. \tag{25}$$

Using (24), we apply the asymptotic homogenisation technique by expressing all the fields in terms of power series of ϵ and accounting for the chain rule (25). This leads to a multiscale system of PDEs, where we can then equate the same powers of ϵ in order to obtain a number of differential conditions which can be used to close a system of PDEs for the leading (zero-th) order fields, or their cell average, defined by

$$\langle q \rangle_j = \frac{1}{|\Omega_j|} \int_{\Omega_j} q(\mathbf{x}, \mathbf{y}, t) dy. \tag{26}$$

Here, j represents either v or t and $|\Omega_j|$ denotes the vessels (interstitial) cell volume portion. The derivation of the model is carried out as in Al Sariri and Penta (2022) by taking into account the differences highlighted in the Remark discussed in Section 2.3.

The macroscale differential equations describing velocities and pressures are analogous to those reported by Al Sariri and Penta (2022) and read

$$\left\langle \mathbf{u}_v^{(0)} \right\rangle_v = -Y_v \nabla_x p_v^{(0)}, \tag{27a}$$

$$\left\langle \mathbf{u}_t^{(0)} \right\rangle_t = -\bar{\kappa} Y_t \nabla_x p_t^{(0)}, \tag{27b}$$

$$\nabla_x \cdot \left(Y_v \nabla_x p_v^{(0)} \right) = \frac{\bar{L} \left(p_v^{(0)} - p_t^{(0)} \right)}{|\Omega_v|} S, \tag{27c}$$

$$\nabla_x \cdot \left(\bar{\kappa} Y_t \nabla_x p_t^{(0)} \right) = \frac{\bar{L} \left(p_t^{(0)} - p_v^{(0)} \right)}{|\Omega_t|} S, \tag{27d}$$

where S is the surface of the microvessels. These differential equations show that the velocities in both compartments obey Darcy's law and the fluid flow depends on the pressure difference between them. The effective coefficients in the above equations are to be computed by solving microscale cell problems. As the microscale problems are those discussed by Al Sariri and Penta (2022), we refer to this work for further details on this matter. However, for the sake of self-consistency and clarity, we have also reported the cell problems related to the auxiliary fields W, **m**, **r**, **a**, **b**, **g**, and **e** in Appendix. The hydraulic conductivity tensors Y_t and Y_v are defined as

$$Y_v = \frac{1}{|\Omega_v|} \int_{\Omega_v} W dy, \quad Y_t = I - \left\langle \left(\nabla_y \mathbf{r}\right)^T \right\rangle_v. \tag{28}$$

The macroscale differential equation for the concentration of nanoparticles $c_v^{(0)}$ can be written as advection–diffusion–reaction equation

$$\frac{\partial c_v^{(0)}}{\partial t} + \nabla_x \cdot \left(c_v^{(0)} \left\langle \mathbf{u}_v^{(0)} \right\rangle_v - F_v \nabla_x c_v^{(0)} \right) + \frac{S}{|\Omega_v|} \bar{\Pi} c_v^{(0)} = 0, \tag{29a}$$

$$\frac{d\Psi^{(0)}}{dt} = \bar{\Pi}_1 c_v^{(0)}, \tag{29b}$$

with diffusivity tensor F_v is described as

$$F_v = \bar{D}_v \left(I - \left\langle \left(\nabla_y \mathbf{a}\right)^T \right\rangle_v \right). \tag{30}$$

Finally, the temperatures $T_t^{(0)}$ and $T_v^{(0)}$ of both compartments at the macroscale are represented by advection–diffusion–reaction equations

$$\frac{\partial T_v^{(0)}}{\partial t} + \nabla_x \cdot \left(T_v^{(0)} \left\langle \mathbf{u}_v^{(0)} \right\rangle_v - N_v \nabla_x T_v^{(0)} \right)$$
$$+ \frac{S}{|\Omega_v|} \bar{\beta}_v \left(T_v^{(0)} - T_t^{(0)} \right) = \bar{\alpha}_v \left(\psi^{(0)} + c_v^{(0)} \right), \tag{31a}$$

$$\frac{\partial T_t^{(0)}}{\partial t} + \nabla_x \cdot \left(T_t^{(0)} \left\langle \mathbf{u}_t^{(0)} \right\rangle_t - N_t \nabla_x T_t^{(0)} \right)$$
$$+ \frac{S}{|\Omega_t|} \bar{\beta}_t \left(T_t^{(0)} - T_v^{(0)} \right) = \bar{\alpha}_t \mathcal{R}^{(0)}. \tag{31b}$$

The effective thermal conductivities N_v and N_t are expressed as:

$$N_v = \bar{K}_v \left(I - \left\langle \left(\nabla_y \mathbf{g}\right)^T \right\rangle_v \right), \quad N_t = \bar{K}_v \left(I - \left\langle \left(\nabla_y \mathbf{e}\right)^T \right\rangle_t \right). \tag{32}$$

The auxiliary tensor W, and the auxiliary variables **r**, **a**, **g**, and **e** solve the microscale cell problems which are described in details in Al Sariri and Penta (2022). The numerical solutions of these problems are illustrated in Penta and Ambrosi (2015) and Mascheroni and Penta (2017).

The difference between the work carried out by Al Sariri and Penta (2022) and the present work resides in the different heat sources which appear in Eqs. (31a) and (31b). These latter also depend on adhesion, which is in turn dictated by Eqs. (29a)–(29b). Here, the nanoparticle dynamics depends on adhesion, as shown by the reaction term in Eq. (29a) and by the macroscale evolution Eq. (29b). This is not the case in the works by Mascheroni and Penta (2017) and Al Sariri and Penta (2022), where nanoparticle transport is governed by a double system of advection–diffusion–reaction equations driven by transvascular exchange of particles which arises as a direct consequence of extravasation, which is herein neglected. In the remainder of this work, we assume that the leading order heat source $\mathcal{R}^{(0)}$ is related to the heat generated by the interaction between the nanoparticles and the magnetic field in the vessels. We can capture the volumetric character of the heat generated by the vessels as a heat source in the tumour tissue by assuming a simple constitutive law for $\mathcal{R}^{(0)}$ of the form

$$\mathcal{R}^{(0)} = c_v^{(0)} + \psi^{(0)}, \tag{33}$$

which is analogous to that present in the vessels and represents an admissible choice as $c_v^{(0)}$ and $\psi^{(0)}$ do not depend on the microscale variable $\mathbf{y}$ and are defined in the whole macroscale domain.

2.6. The homogenised model in radial symmetry

The vascularised tumour is represented by a sphere of radius R. We assume that the tumour is isolated and all external forces are neglected. The radial component of fluid velocities and pressures are those obtained by Penta and Ambrosi (2015). The system of equations in spherical coordinates, by considering the leading order term for all variables (and neglecting the superscript $^{(0)}$ for the sake of simplicity of notation) reads

$$\frac{\partial c_v}{\partial t} + \frac{1}{r^2}\frac{\partial}{\partial r}\left(r^2\left(c_v\langle\mathbf{u}_v\rangle_v - \mathsf{F}_v\frac{\partial c_v}{\partial r}\right)\right)$$
$$+ \frac{S}{|\Omega_v|}\bar{\Pi}c_v = 0 \quad \text{in} \quad \Omega_v, \tag{34a}$$

$$\frac{d\Psi}{dt} = \bar{\Pi}_1 c_v \quad \text{in} \quad \Omega_v, \tag{34b}$$

$$\frac{\partial T_v}{\partial t} + \frac{1}{r^2}\frac{\partial}{\partial r}\left(r^2\left(T_v\langle\mathbf{u}_v\rangle_v - \mathsf{N}_v\frac{\partial T_v}{\partial r}\right)\right)$$
$$+ \frac{S}{|\Omega_v|}\bar{\beta}_v\left(T_t - T_v\right) = \bar{\alpha}_v\left(c_v + \psi\right) \quad \text{in} \quad \Omega_v, \tag{34c}$$

$$\frac{\partial T_t}{\partial t} + \frac{1}{r^2}\frac{\partial}{\partial r}\left(r^2\left(T_t\langle\mathbf{u}_t\rangle_t - \mathsf{N}_t\frac{\partial T_t}{\partial r}\right)\right)$$
$$+ \frac{S}{|\Omega_t|}\bar{\beta}_t\left(T_v - T_t\right) = \bar{\alpha}_t\left(c_v + \psi\right) \quad \text{in} \quad \Omega_t. \tag{34d}$$

All variables depend on r and t, where $0 \leq r \leq R$ and $0 \leq t \leq \mathcal{T}$.

To close the problem, we need to prescribe the initial and boundary conditions. We assumed zero concentration and due to the spherical symmetry, we consider zero flux of nanoparticles' concentration at the centre of the tumour. We assume that the particles are delivered intravascularly for a time σ which means that the concentration is c_n during this time and zero after that,

$$c_v|_{t=0} = 0, \tag{35a}$$

$$\left(\mathbf{u}_v c_v - \bar{D}_v\partial_r c_v\right)\Big|_{r=0} = 0, \tag{35b}$$

$$c_v|_{r=R} = \begin{cases} c_n & t < \sigma, \\ 0 & t > \sigma. \end{cases} \tag{35c}$$

Concerning heat transport, we set initial ($t = 0$) temperatures in both compartments to the standard blood temperature. In terms of boundary conditions, we consider zero heat flux at $r = 0$. On the tumour boundary, We prescribe the homogenised temperature in the vessels to coincide with the standard blood temperature, while we consider a Robin condition for the tumour temperature $r = R$, to account for the heat transport between the tumour interstitial and vessels compartments mediated by intermediate layer of external tissue, as in Nabil and Zunino (2016) and Al Sariri and Penta (2022). Initial and boundary conditions for the heat transport system of equations are given below.

$$T_v|_{t=0} = T_t|_{t=0} = 1, \tag{36a}$$

$$\left(\mathbf{u}_v T_v - \bar{K}_v\frac{\partial T_v}{\partial t}\right)\Big|_{r=0} = \left(\mathbf{u}_t T_t - \bar{K}_t\frac{\partial T_t}{\partial t}\right)\Big|_{r=0} = 0, \tag{36b}$$

$$T_v|_{r=R} = 1, \qquad \left(\mathbf{u}_t T_t - \bar{K}_t\frac{\partial T_t}{\partial t}\right)\Big|_{r=R} = \bar{\beta}_t(T_v - T_t). \tag{36c}$$

In this manuscript, we are consistent with the boundary conditions utilised in Nabil and Zunino (2016) and Al Sariri and Penta (2022). Our set of conditions represents a situation where the nanoparticles are first injected for a period of time, cf. (35c), and then the magnetic field is subsequently applied, so that the temperatures distributions are then driven by heat sources which depend on the absorption rate and concentration of nanoparticles, cf. (31a)–(31b), and the heat transport problem is then closed by initial conditions (36a) and boundary conditions (36b)–(36c). The present problem at hand is very rich, and that future investigations on the subject could also focus on different initial and/or boundary conditions.

The hydraulic conductivity, diffusivity, and thermal conductivity coefficients are computed as discussed in Al Sariri and Penta (2022), based on the microscale simulations performed in Penta and Ambrosi (2015) and Mascheroni and Penta (2017). The resulting values are then injected in our macroscale system of PDEs, and we use the values of the parameters in Table 1 to solve the model and present the results.

3. Results and discussion

Penta and Ambrosi (2015) discussed the solution of the fluid flow system (27a)–(27d) and they determined the radial components of the velocities and pressures which were used to find the particles' concentration and heat convection as investigated by Mascheroni and Penta (2017), and Al Sariri and Penta (2022). The authors of the mentioned works studied the influence of the geometry of the microvessels on the distribution of the particles and they concluded that vessels' tortuosity impairs the transport of fluid (Penta and Ambrosi, 2015), particles (Mascheroni and Penta, 2017), and heat (Al Sariri and Penta, 2022). Here, the differential Eqs. (34a)–(34d), equipped with initial and boundary conditions (35a)–(35c), and (36a)–(36c), are solved via the finite element software COMSOL Multiphysics as in Al Sariri and Penta (2022). The plots illustrating spatio-temporal temperatures and concentration profiles in Section 3.1 are generated using COMSOL Multiphysics, while Python is used to generate the plots related to the parametric analysis discussed in Section 3.2.

Remark (*Presentation of the Results*). While we solve the model in non-dimensional form, results in terms of temperatures and concentrations are presented by referring to their corresponding dimensional values in the plots in order to foster the Reader's understanding. In particular, temperatures are expressed in degree Kelvin (K), and concentrations in mg/ml (or, equivalently kg/m^3).[1] The non-dimensional time unit in this work can be computed by means of relationship (18) and corresponds to 50 s. This applies when we discuss conditions related to time intervals in dimensional form in the following sections. For example, it means that an injection time of 50 min corresponds to 60 non-dimensional time units. The radius and the time are expressed in non-dimensional form in the following sections. Therefore, the non-dimensional radius ranges from 0 to 1, while the chosen time interval is from 0 to 1000, which corresponds to a time interval of $5 \cdot 10^4$ s ($\approx$13.88 h).

3.1. The role of vessels' tortuosity

We commence by investigating the role of the microvascular tortuosity on the concentration of nanoparticles in Section 3.1.1 and on the resulting temperature maps in Section 3.1.2. The results are shown in terms of vessels' concentration c_v, density ψ, and tumour temperature T_t vs relative radius of the homogenised tumour or time. We have conducted the analysis by labelling the microstructures at varying tortuosities with the index λ. The latter actually corresponds to a specific couple of spatial frequency ω and amplitude A, as specified in Table 2, and are those used in Penta and Ambrosi (2015), Mascheroni and Penta (2017) and Al Sariri and Penta (2022) to parametrise the tumour microvessels. Each of these couple of parameters determine a different microstructure, with their associated vessels surface and corresponding cell volume portion. Given that we are focussing on the microvasculature considered by Penta and Ambrosi (2015), invariance with respect to mutual orthogonal axis applies. As such, the effective hydraulic conductivities, as well as drug and thermal diffusivities, are isotropic and their values at varying tortuosities are listed in Table 2. These are denoted by $H_v = \langle\mathsf{W}_{11}\rangle = \langle\mathsf{W}_{22}\rangle = \langle\mathsf{W}_{33}\rangle$ for the hydraulic

---

[1] In this latter case no rescaling is needed as the reference concentration is 1 mg/ml.

Table 1
Values of model parameters.

| Symbol	Parameter	Value	Unit	Reference
τ_0	Larmor time constant	10^{-9}	s	De la Presa et al. (2012)
k_i	Magnetic anisotropy constant	1.1×10^4	J/m^3	Ferguson et al. (2013)
K_B	Boltzmann constant	1.38×10^{-23}	J/K	Ferguson et al. (2013)
η	Nanoparticles' carrier liquid viscosity	2.94×10^{-4}	kg/m s	Torres et al. (2019)
z	Adhesion probability	1.5×10^{-4}	Non	Nabil and Zunino (2016)
μ	Blood viscosity	4×10^{-3}	Pa s	Nabil and Zunino (2016)
L_p	Vessel hydraulic permeability	1.78×10^{-11}	m/Pa s	Jain et al. (2007)
k	Tumour hydraulic conductivity	2.1×10^{-13}	m^2/Pa s	Boucher et al. (1998)
D_v	The diffusivity of nanoparticles in the capillaries	3.3×10^{-10}	m^2/s	Shipley and Chapman (2010)
D_t	The diffusivity of nanoparticles in the tissue	1.0×10^{-11}	m^2/s	Shipley and Chapman (2010)
K_t	Thermal conductivity at tissue	0.52	W/m K	Tang et al. (2018)
K_v	Thermal conductivity at vessel	0.51	W/m K	Tang et al. (2018)
β	Heat transfer coefficient	20	W/m^2 K	Nabil and Zunino (2016)
L_c	Membrane permeability related to the drug	1.7×10^{-7}	m/s	Modok et al. (2006)
d	Reference microscale	4.0×10^{-5}	m	Less et al. (1997)
L	Reference macroscale	1.0×10^{-2}	m	Jain et al. (2007)
C	Reference pressure gradient	5×10^2	Pa/m	Shipley and Chapman (2010)
γ_t	Tissue-specific heat	3470	J/kg K	Nabil and Zunino (2016)
ρ_t	Tissue density	1060	kg/m^3	Nabil and Zunino (2016)
γ_v	Vessels-specific heat	3617	J/kg K	Miaskowski and Sawicki (2013)
ρ_v	Vessels density	1050	kg/m^3	Miaskowski and Sawicki (2013)
C_r	Concentration reference	1	mg/ml	De la Presa et al. (2012)
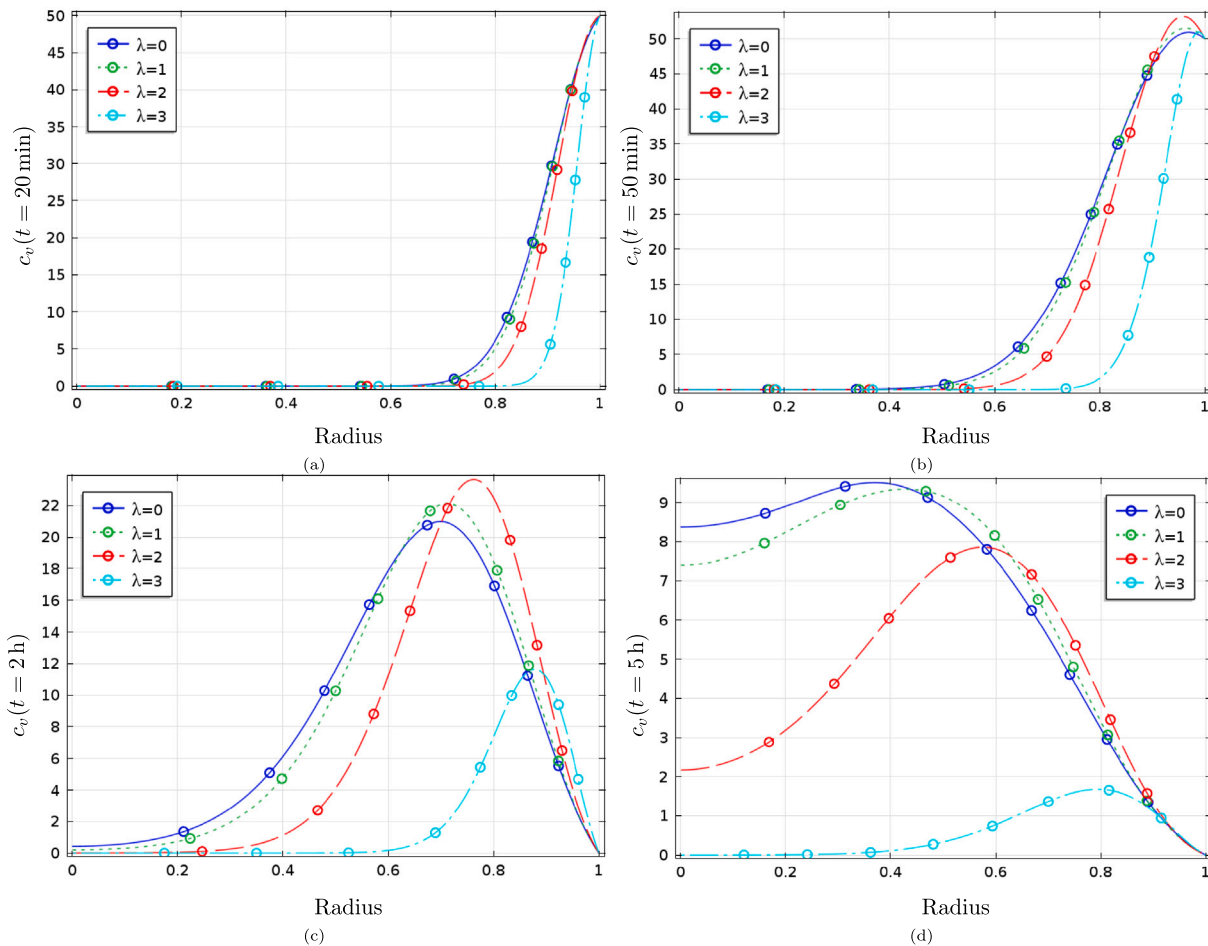
Fig. 2. The concentration of nanoparticles c_v as a function of tumour radius r for various values of vessels' tortuosity as specified in the legends and for time moment (a) $t = 20$ min (b) $t = 50$ min (c) $t = 2$ h and (d) $t = 5$ h. All other parameter values are as specified in Table 1 except for the parameters $\sigma = 50$ min, and $c_n = 50$ mg/ml.

conductivity, whereas the homogenised thermal and drug diffusivities are to be computed by simply multiplying their corresponding non-dimensional values by the correction factor herein denoted by $1 - \left\langle \frac{\partial a,g}{\partial y_1} \right\rangle_v$, which was computed for the considered microstructures

by Mascheroni and Penta (2017). We also assume that, given the low vascular density, the interstitial hydraulic conductivity and thermal diffusivities are unaffected by the homogenisation process, as justified in Penta and Ambrosi (2015).

Table 2
Particle diffusivity and thermal conductivity values for various vessel geometry.

λ	ω	A	$|\Omega_v|$	$|\Omega_t|$	S	H_v	$1 - \left\langle \frac{\partial a, g}{\partial y_1} \right\rangle_v$
0	0	0	$8.1 \cdot 10^{-2}$	6.149	2.30	$2.20 \cdot 10^{-4}$	$3.6 \cdot 10^{-1}$
0.5	1	$0.5 r_c$	$7.9 \cdot 10^{-2}$	6.151	2.30	$2.06 \cdot 10^{-4}$	$3.53 \cdot 10^{-1}$
1	1	r_c	$7.6 \cdot 10^{-2}$	6.154	2.32	$1.69 \cdot 10^{-4}$	$3.19 \cdot 10^{-1}$
1.5	2	$0.5 \, r_c$	$7.6 \cdot 10^{-2}$	6.154	2.33	$1.63 \cdot 10^{-4}$	$3.18 \cdot 10^{-1}$
2	2	r_c	$6.9 \cdot 10^{-2}$	6.161	2.57	$6.24 \cdot 10^{-5}$	$2.13 \cdot 10^{-1}$
2.5	3	$0.5 \, r_c$	$7.2 \cdot 10^{-2}$	6.158	2.53	$7.71 \cdot 10^{-5}$	$2.47 \cdot 10^{-1}$
3	3	r_c	$6.5 \cdot 10^{-2}$	6.165	3.25	$4.89 \cdot 10^{-6}$	$0.9 \cdot 10^{-1}$

Table 3
Properties of magnetic nanoparticles.

Material	M_d (kA/m)	ρ_n (kg/m³)	Reference
$Fe_3 O_4$	446	5180	Kappiyoor et al. (2010)
fcc Fe Pt	1140	15 200	Kappiyoor et al. (2010)
Ba $Fe_2 O_4$	380	5280	Kappiyoor et al. (2010)
Ni Fe	301	5380	Ng et al. (2017)

3.1.1. Concentration of nanoparticles

The result of the differential equations (34a)–(34b) with initial and boundary conditions (35a)–(35c), is the homogenised concentration of particles in the vessels, which reflects the effective behaviour of the nanoparticles delivered intravascularly in a macroscale spherical tumour.

A concentration of 50 mg/ml of magnetic nanoparticles is injected for a time $\sigma = 50$ min. Fig. 2 shows the concentration of nanoparticles at different times both during and after injection. It is clear that during the injection phase, the concentration on the boundary of the tumour is very high but cannot influence regions far from the boundary. When we stop injecting the nanoparticles at $t > 50$ min, the particles start to diffuse more towards the tumour centre. Also, in all cases highlighted in Fig. 2 it is clear that tortuosity has a negative impact of nanoparticles transport, although intermediate values of the tortuosity may lead to optimal concentration peaks post injection, as in case of Fig. 2c, where the highest concentration peak is reached at $\lambda = 2$ and after injection at $t = 2$ h. The vessels with tortuosity $\lambda = 0$ and $\lambda = 1$ correspond to approximately similar concentration of nanoparticles profiles, and the maximum is reached approximately after 6 h, see Fig. 3. In contrast, the concentration is very low for the most tortuous vessels at $\lambda = 3$. This is because the nanoparticles are advected by the fluid and for very high tortuosity the fluid flow is dramatically impaired and no longer characterised by a parabolic profile. This ultimately causes a sharp decline in the hydraulic conductivity of the vessels, as explained by Penta and Ambrosi (2015). These obtained profiles are in qualitative agreement with those obtained by Mascheroni and Penta (2017) and Al Sariri and Penta (2022). However, there are discrepancies between our results and previous results in terms of the amount of concentration and the time that it takes for the nanoparticles to reach the centre due to the difference in boundary conditions and the presence of adhesion which is neglected in Al Sariri and Penta (2022).

Mascheroni and Penta (2017) and Al Sariri and Penta (2022) dealt with drug delivered by a bolus injection accounting for an exponential decline in the concentration of nanoparticles due to plasma clearance, therefore, they observed a slower drug dynamics. In our case, the injected concentration of nanoparticles on the boundary of the tumour drops to zero directly after 50 min, and so the drug can reach the tumour centre regions by diffusive transport after a few hours post-injection.

We chose an injection time of 50 min to be consistent with the experiment performed by Famiani et al. (2018), and we also test different injection times in the course of the parametric analysis in Section 3.2.

We conclude this section by discussing the role of the density of nanoparticles Ψ adhering to the vessels' walls. Its maximum is reached close to the domain boundary, and it depends on the tortuosity of the vessels, see Fig. 3. Moreover, if we compare the profile of c_v and Ψ with different vessels' tortuosity, we can see that the peak in the case of Ψ, as well as c_v 2 h post-injection, is reached at $\lambda = 2$. This is because, while tortuosity impairs fluid convection, the adhesion of nanoparticles is supposed to increase at increasing tortuosity due to the friction between the particles and the vessels. Therefore, we suggest that, while tortuosity is in general negatively affecting nanoparticles' transport

as in Mascheroni and Penta (2017) and Al Sariri and Penta (2022), whenever adhesion is taken into account, less regularisation of the vessels' may be required to achieve optimal nanoparticles' transport. However, at $\lambda = 3$, transport still drops dramatically, as in this case the increase in nanoparticle adhesion is not sufficient the counterbalance the drop in fluid, and hence nanoparticles advection.

Finally, we also wish to remark that the concentration is prescribed as a time-dependent boundary (rather than initial) condition and injected over a period of time, such that there exists a transient period before the drug is cleared off when localised regions in space can develop where the concentration exceeds the boundary value. This can be seen by observing the concentration profile in Fig. 2(b) at $\lambda = 2$. This phenomenon typically happens when the time is still comparable to the injection time σ. For a shorter period of time the concentration delivered to the system is typically not sufficient for this to occur. For a time much longer than the injection time the concentration is already significantly lower than the boundary value being prescribed during the injection time.

3.1.2. Temperature maps

The differential equations (34c)–(34d) with boundary and initial conditions (36a)–(36c) are used to find the heat maps for a vascularised tumour. As mentioned in Section 2, the hyperthermia effectiveness depends on the absorption rate α, which is in turn affected by both the properties of the magnetic field, such as intensity and frequency, as well as the properties of the magnetic nanoparticles. Abenojar et al. (2016) found that theoretically and experimentally the absorption rate of cubic nanoparticles is higher than the spherical nanoparticles and nano-rods are better than cubic and spherical nanoparticles (Das et al., 2016). However, for the sake of simplicity, in this work we focus on spherical particles and we show that cancer hyperthermia can be improved by changing nanoparticles' material, size, concentration, and also the injection duration time. Varying the material of nanoparticles requires to change their magnetisation M_d and their density ρ_n, see Table 3. The parameter M_d is more relevant than others in the way it affects the absorption rate α as the latter is proportional to the square of M_d and inversely proportional to ρ_n. Fig. 4(b) shows that (FePt) responds with higher temperature changes when compared with other materials typically considered in this context. Usually the magnetisation of metallic nanoparticles like Iron–Platinum (FePt), Iron–Cobalt (FeCo), Cobalt–platinum (CoPt) is higher than the oxidation nanoparticles like Iron-Oxide (FeO), Maghemite (Fe_2O_3), and Magnetite (Fe_3O_4), but the former are not stable (Gubin, 2009). As such, in the present work we concentrate more on magnetite nanoparticles, as appropriate for application of cancer hyperhermia to human tissues (Hergt et al., 2006). Fig. 4(a) shows the temperature profile arising from injection of magnetite nanoparticles with different vessels' tortuosity. The concentration of particles drives heat transport from the boundary towards the tumour centre. Convection–diffusion of heat then causes the temperature to raise from the standard blood temperature, which is prescribed at the tumour boundary, to higher values. Microvascular tortuosity is associated with a reduce increase in temperature, in agreement with previous findings reported for heat transport driven by small nanoparticles discussed by Al Sariri and Penta (2022) Moreover, the temperature increases and approaches its maximum after approximately 2.5 h, then it starts to decrease as the overall concentration declines.
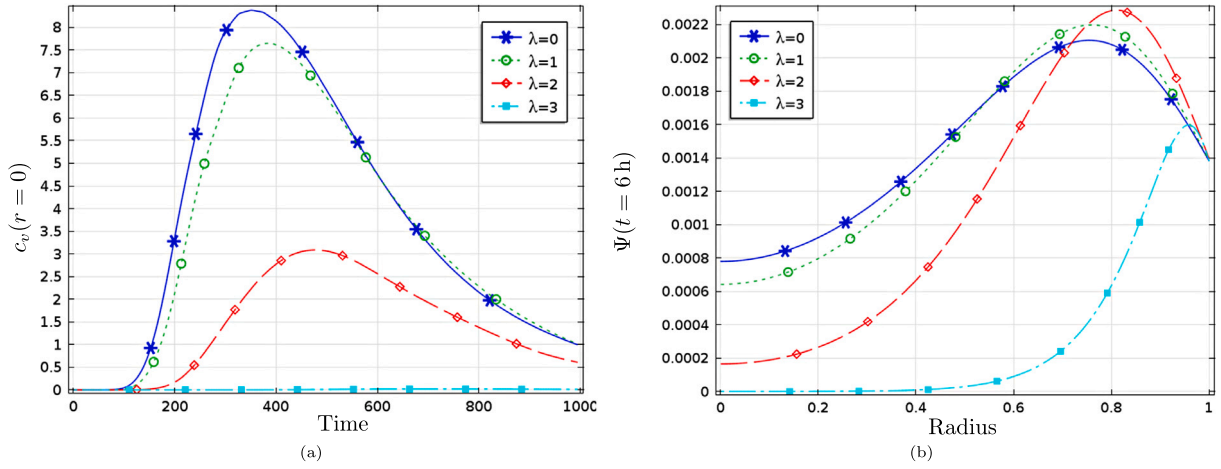
Fig. 3. The concentration of nanoparticles vs time, and the density of nanoparticles that adheres to the vessels' wall vs the radius of tumour. (a) Instantaneous concentration of nanoparticles c_v at the center of tumour $r = 0$ as a function of time for various values of vessel tortuosity as specified in the figure legends. (b) Instantaneous density of nanoparticles Ψ that adheres to the wall of the vessels as a function of tumour radius for different tortuosity of the vessels. In both panels the time point is $t = 6$ h. All other parameters are as specified in Tables 1 and 2 except $\sigma = 50$ min, and $c_n = 50$ mg/ml.
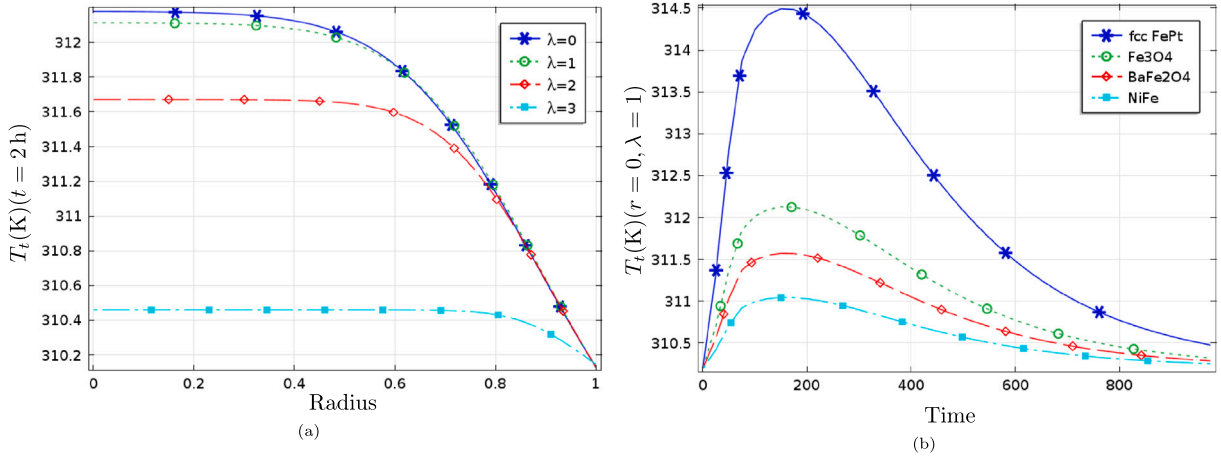
Fig. 4. (a) Instantaneous tumour temperature T_t at time $t = 2$ h as a function of tumour radius r for Fe_3O_4 nanoparticles and various values of vessel tortuosity as specified in the figure legend. (b) Local tumour temperature T_t at the centre of the tumour $r = 0$ as a function of time for various types of nanoparticles materials as specified in the figure legends and for vessels with tortuosity $\lambda = 1$. All other parameter values are as specified in Table 1 except for the parameters $H_0 = 10$ kA, $f = 300$ kHz, $\sigma = 50$ min, and $c_n = 100$ mg/ml.

The remainder of this section is devoted to a parametric analysis which is performed to determine the optimal set of parameters (including injection conditions, magnetic field properties, nanoparticles' diameter, microvessels' tortuosity, wall shear rate) which is required to reach a physiologically safe target hyperthermic temperature and duration.

3.2. A parametric study of hyperthermic temperature and duration

The ranges in which the hyperthermic temperature and duration take safe and effective values depend strongly on the pathophysiology of the tumour tissue under treatment. For this reason, the published literature gives various estimates of these quantities — see the Introduction for further discussion. Table 4 summarises values of the target hyperthermic temperature and duration suggested in several clinical and experimental investigations. Based on the data in Table 4, we assume that the safe and effective values for the hyperthermic temperature are in the range $[42°, 46°]$C and the safe and effective hyperthermic duration has values in the range $[0.5, 2]$ h. Below these intervals hyperthermia treatment does not induce sufficiently strong sensitisation to radiotherapy and chemotherapy or lead to significant direct thermal ablation of cancer cells. Above these intervals undesirable damage to healthy tissue occurs.

Fig. 5 demonstrates how the value of the hyperthermic duration is computed from the numerical results of our model. A typical example of the temperature profile as a function of time in the centre of the tumour, $r = 0$. is shown in the Figure for fixed values of the model parameters. Initially, the temperature increases monotonically and eventually reaches the hyperthermic temperature, $T_t = 42$ °C, after an initial transient time as shown by the horizontal green line in Fig. 5. The temperature continues to increase further until it reaches a single global maximum $T_{\max}$ and decreases monotonically after that until it eventually drops below the hyperthermic temperature. The hyperthermic duration is defined and computed as the difference between the moment in time when the temperature decreases below the hyperthermic temperature of 42 °C and the moment in time when the temperature first exceeds this value. These moments are indicated in Fig. 5 by vertical red lines. The hyperthermic duration is denoted by τ for the remainder of this section.

Fig. 6(a) shows a 3D plot of the hyperthermic duration τ as a function of the intensity of the applied magnetic field H_0 and the nanoparticle injection duration σ for all other model parameters fixed at constant values. For small values of H_0 and σ the hyperthermic duration is zero as the $T_{\max}$ has not yet exceeded the hyperthermic temperature of 42 °C. As the values of H_0 and σ are increased, either separately or simultaneously, the hyperthermic temperature of 42 °C

Table 4
Estimates for the hyperthermic temperature and duration available from the published literature.

Temperature (°C)	Duration (min)	Reference
44	30	Kawai et al. (2008)
42.5	60	Perez and Sapareto (1984)
41.5	120	Sakaguchi et al. (1995)
42	30	Pankhurst et al. (2003)
41	60	Dudar and Jain (1984)
47	30	Hilger (2013)
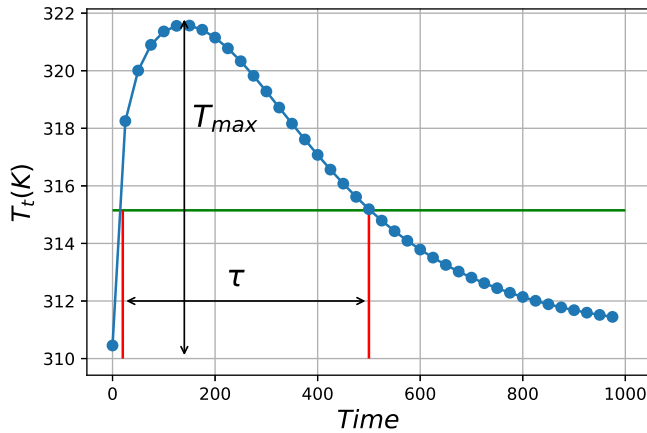
Fig. 5. Temperature T_t at the middle of the tumour ($r = 0$) as a function of time in the case of vessels with tortuosity $\lambda = 1$ and all other parameter values are as in Table 1 except $H_0 = 10$ kA, $f = 300$ kHz, $\sigma = 50$ min, $c_n = 100$ mg/ml, $\xi = 15$, and $pd = 80$ nm. The two vertical red lines indicate the hyperthermic duration τ - the time interval for which the tumour temperature profile exceeds the hyperthermic temperature $T_t = 42\,°C$ shown with a horizontal green line.

is eventually exceeded and a non-vanishing value of the hyperthermic duration τ is recorded and continue to increase monotonically with increase of both H_0 and σ. The range of safe and effective hyperthermic duration values are then the values on the surface $\tau(H_0, \sigma)$ that are located between the iso-contour lines $\tau = 0.5$ h and $\tau = 2$ h. These isolines are shown by a red solid curve and a red dashed curve in the plot of Fig. 6(a). Fig. 6(b) shows a similar surface plot of the maximal (in time) temperature at the centre of the tumour $r = 0$ as a function of H_0 and σ for all other model parameters fixed at constant values again. The surface is monotonically increasing, and the safe and effective range of temperature values is the one located between the iso-contours $T_{\max} = 42\,°C$ and $T_{\max} = 46\,°C$. These iso-contours are shown by green dash-dotted and green dotted lines in the Figure. Fig. 6(c) shows the projections of the safe and effective iso-contour lines $\tau = 0.5$ h and $\tau = 2$ h determined from Fig. 6(a) and the safe and effective iso-contour lines $T_{\max} = 42\,°C$ and $T_{\max} = 46\,°C$ determined from Fig. 6(b) onto the coordinate plane (H_0, σ) that they all have in common. For successful hyperthermia treatment both the hyperthermic temperature and the hyperthermic duration must be within their safe and effective ranges. Hence, we conclude that for fixed other parameter values, the values of the intensity of the applied magnetic field H_0 and the nanoparticle injection duration σ must be chosen within the intersection of the two regions thus determined. The resulting estimate of safe and effective values (H_0, σ) are shown as a shaded region in Fig. 6(c).

The procedure described in relation to Fig. 6 can be applied similarly to other pairs of model parameters. Fig. 7 shows the regions of safe and effective hyperthermia treatment in the parameter planes (H_0, c_n), (H_0, pd), (ξ, H_0), and (λ, H_0), where λ is tortuosity of the vessels, pd is the diameter of nanoparticles, ξ is the wall shear rate, c_n is the injected concentration of particles at the boundary and H_0 is the magnetic field intensity . The latter is used as a common axis in order to make easier to cross-reference further parameter pairs. Figs. 6(c) and 7 constitute a

major result of our analysis. They may be used to design and optimise hyperthermia procedures. Further discussion of these results is included in the next section.

4. Conclusion

We have solved a new system of homogenised PDEs which models cancer hyperthermia in solid tumours driven by magnetic heating of large nanoparticles. The model is obtained by applying the asymptotic homogenisation technique, as done in the recent work proposed by Al Sariri and Penta (2022), where the role of microvascular tortuosity on heat transport driven by small nanoparticles is investigated.

The resulting governing equations in this work describe fluid transport and its exchange between the interstitial tumour space and the micro-vessels, as well as nanoparticles transport. The latter is assumed to occur solely in the vessels to which particles can adhere, as opposed to the work by Al Sariri and Penta (2022), where extravasation of small nanoparticles was taken into account, and adhesion ignored. We have performed a parametric analysis to study the role of nanoparticles and applied magnetic field properties, as well as micro-vessels tortuosity, on the temperature reached as a consequence of cancer hyperthermia (*hyperthermic temperature*), as well as the duration for which this latter is maintained (*hyperthermic duration*).

This way, we have identified the optimal cancer hyperthermia parameters for safe and effective hyperthermic temperature and duration conditions (herein identified in $42 - 46\,°C$ for 30 min to 2 h). The main results of our analysis are shown in Figs. 6 and 7 in terms of particles' diameter, magnetic field intensity, vessels' shear rate, injection conditions (injected concentration and duration), as well as microvascular tortuosity.

According to our results, both the injected concentration of nanoparticles, and the time during which they are administrated, play a prominent role in reaching the desired hyperthermic conditions. The safe magnetic field intensity to be applied increases monotonically with decreasing injection time and duration, as expected.

The role of particles' diameter in the investigated range only weakly affects the safe range of magnetic intensity. On the other hand, we find that the properties of the microvessels play a crucial role in determining the hyperthermic conditions of the system.

Increasing the wall shear rate requires a corresponding increase in magnetic field intensity, although such an increase exhibits a sublinear profile. This may be due to the fact that, on the one hand, the wall shear rate determines an increase in the particles' density adhering to the vessels' walls and hence an increase in the heat source directly related to adhesion. On the other hand, an increase of the adhesion also translates in particle absorption at the macroscopic scale, so that, in turn, part of the nanoparticles flowing in the vessels are uptaken thus causing a net decrease in the heat source, as the latter also depend on the actual concentration of nanoparticles. In the scenario at hand, the latter phenomenon overtakes the former, as the concentration affects the heat source more than the density of nanoparticles adhering to the vessels, thus justifying the obtained profile.

The role of microvessels' tortuosity is in agreement with the findings reported in Al Sariri and Penta (2022), in that in general, regularisation of the tumour microstructure leads to an overall improvement in fluid, drug, and ultimately heat transport. However, high concentration peaks can be reached for intermediate values of the tortuosity, due to the fact that increasing the geometrical complexity of the vessels' leads to consequences which can potentially lead to opposite effects on the drug and heat dynamics.

In fact, an increased tortuosity leads to larger vessel surface, which leads to an increase in adhesion, and, at the same time, to impaired (reduce) fluid, drug, and heat convection. However, the importance of geometric regularisation in enhancing anti-cancer therapies based on drug transport for vascularised tumours is evident also in this current
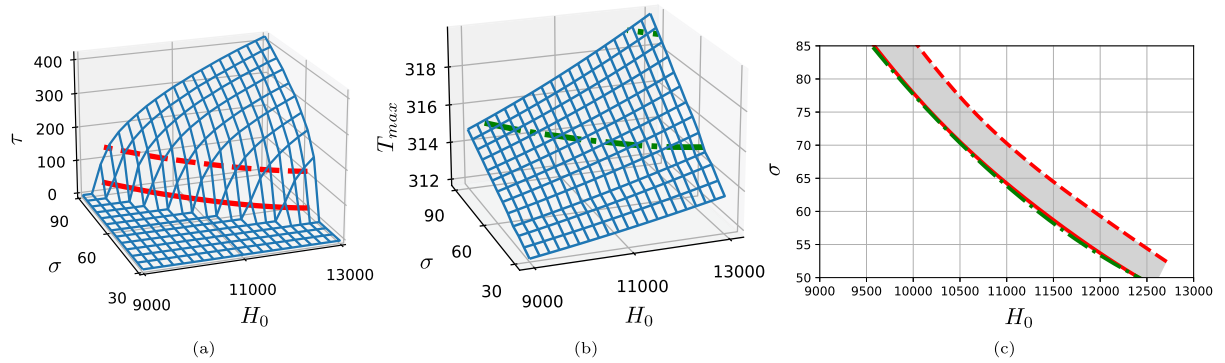
Fig. 6. Surfaces of the hyperthermic duration $\tau(H_0, \sigma)$ in (a) and the maximal temperature at the centre of the tumour $T_{max}(H_0, \sigma)$ in (b) both shown as functions of magnetic field intensity and nanoparticle injection duration. The two red lines in (a) show the range of durations for safe and effective treatment between $\tau = 0.5$ h and $\tau = 2$ h. Similarly the two green lines indicate the range of safe and effective hyperthermic temperature range $42 - 46$ °C. Panel (c) shows the projections of these safe and effective isocontours onto the (H_0, σ) plane and the shaded region being the intersection where both the hyperthermic temperature and duration are within the target ranges. All other parameter values are kept fixed at values specified in Table 1 except $f = 300$ kHz, $\sigma = 50$ min, $c_n = 100$ mg/ml, $\xi = 15$, $pd = 80$ nm.
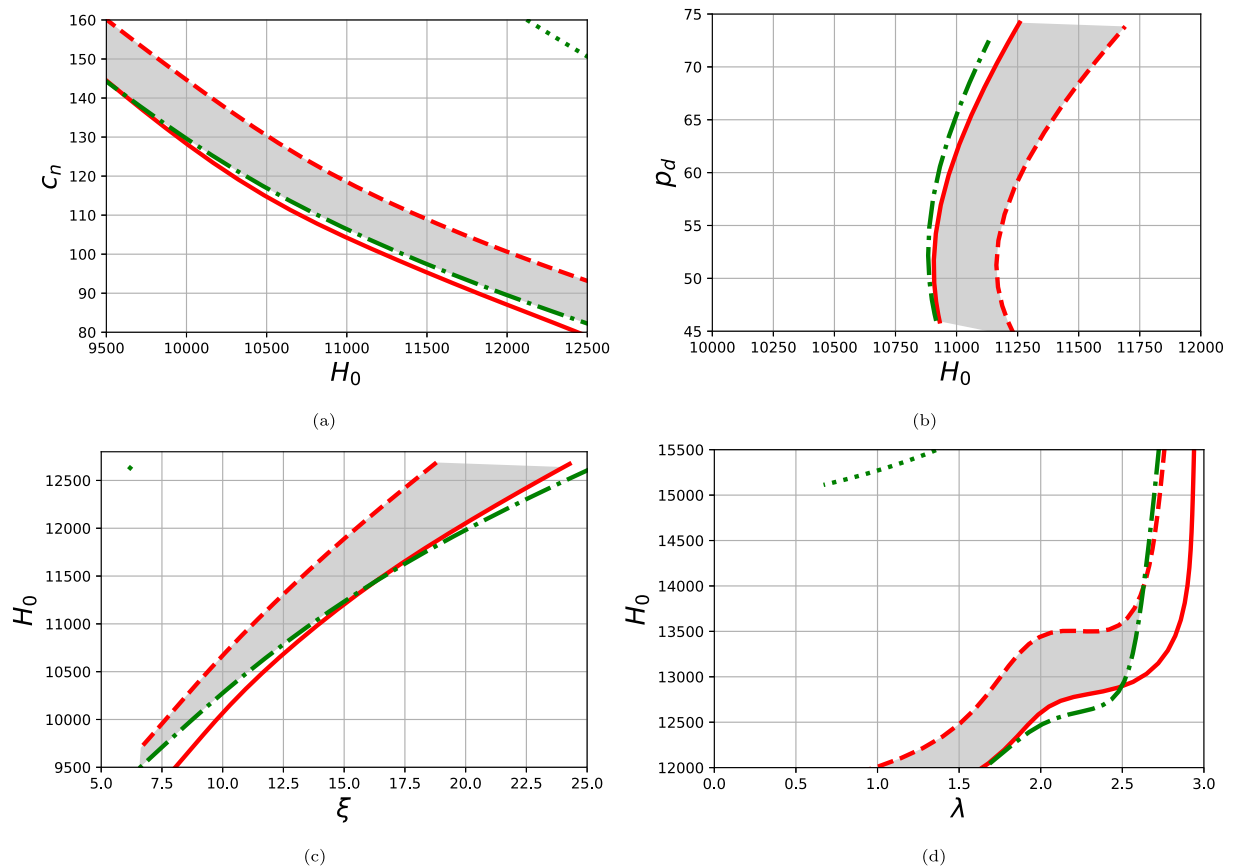

Fig. 7. Regions of safe and effective hyperthermia treatment in the parameter space of the model. The regions are constructed as described in the caption of Fig. 6 and are as follows (a) (H_0, c_n), (b) (H_0, pd), (c) (ξ, H_0), and (d) (λ, H_0). In each panel, all parameters except the ones on the axes are kept fixed at values specified in Table 1 and $f = 300$ kHz, $\sigma = 50$ min, $c_n = 100$ mg/ml, $\xi = 15$, $pd = 80$ nm. The particles' diameter on the ordinate in figure (b) is in nm.

work and in agreement with the works developed by Mascheroni and Penta (2017) and Al Sariri and Penta (2022).

The present work is open for improvements. We have assumed that the tumour does not deform, while of course tissue deformations and growth take place (see also Penta et al., 2014; Penta and Merodio, 2017 where homogenised models for avascular appositional growth an fluid transport in deformable vascular tumours are investigated) and can determine significant consequences on drug transport. In addition, in this work we have assumed a constant wall shear rate for the sake of simplicity, while this is indeed depending on the micro-scale

fluid transport in the vessels. Incorporating the latter could lead to a more realistic description of the influence of adhesion on nanoparticles transport and on its consequences on heat transport. This way, more realistic predictions could be made concerning the necessary geometric regularisation that should be carried out to achieve safe hyperthermic conditions.

We have also ignored the explicit interaction between the tumour and the surrounding healthy tissue and solely focussed on the cancerous region in this particular manuscript. At present, we have adopted the simplified approached proposed in Nabil and Zunino (2016) and also

adopted in Al Sariri and Penta (2022), so that we assume that heat exchange between the vessels and the tumour is mediated by the role of intermediate layers of tissue, and represents this feature by means of the Robin boundary condition (36c). However, in order to formulate more accurate predictions concerning safe hyperthermic conditions, future development of this work should take this interplay explicitly into account, for example by considering the healthy tissue as an individual compartment, as done by Penta et al. (2021) in the context of active porous media.

Furthermore, the potential for vascular collapse (see, e.g., the work by Horsman (2006)) due to tissue overheating should also be taken into account when determining safe hyperthermic conditions.

The current modelling approach can be applied to specific kind of tumours, experimental setups, and physiological symptoms in order to formulate predictions concerning the optimal hyperthermic conditions in the context of cancer hyperthermia. In particular, we have performed a parametric analysis in terms of injection conditions (concentration and duration), particle diameter, magnetic field intensity, wall shear rate, and tortuosity of the microvessels. While some of the parameters, such as injection conditions, magnetic field intensity (and frequency), as well as magnetic particles geometrical properties (including the diameter) can certainly be tuned to optimise hyperthermic conditions, as described for example in the works by Salloum et al. (2008), Kim et al. (2008) and Sawtarie et al. (2017), respectively (alongside many others), others depend on the hydrodynamic conditions at hand and on the specific tumour type. This is the case for parameters such as fluid velocity and wall shear rate, as per the analysis reported by Hossain et al. (2013) and for geometrical properties of the microstructure, see, e.g., Sweeney et al. (2019). As such, we suggest that the optimal way to utilise the modelling approach presented here is to obtain the microvessels' tortuosity based on numerical simulations performed on microstructures parametrised on the basis of real medical images. This way, the other parameters can be tuned to achieve desired hyperthermic conditions that ensure patient safety and effective treatment. Our model and findings contribute to the design of patient-specific diagnostic tools and may help improve the efficacy of current anti-cancer therapies.

CRediT authorship contribution statement

Tahani Al Sariri: Writing – original draft, Formal analysis, Software, Visualisation, Writing – review & editing. **Radostin D. Simitev:** Software, Writing – review & editing, Conceptualisation, Methodology, Supervision, Project administration. **Raimondo Penta:** Software, Writing – review & editing, Conceptualisation, Methodology, Supervision, Project administration.

Declaration of competing interest

The authors declare that they have no known competing financial interests or personal relationships that could have appeared to influence the work reported in this paper.

Data availability

No data was used for the research described in the article.

Acknowledgements

Appendix. The macroscale coefficients

The hydraulic conductivity tensors, diffusion tensors, and thermal conductivity tensors, can be computed by solving appropriate microscale cell problems, see also the work by Al Sariri and Penta (2022).

The hydraulic conductivities Y_v and the second rank tensor Y_t are defined as

$$\mathsf{Y}_v = \langle \mathsf{W} \rangle_v = \frac{1}{|\Omega_v|} \int_{\Omega_v} W \, dy, \tag{A.1}$$

$$\mathsf{Y}_t = I - \frac{1}{|\Omega_t|} \int_{\Omega_t} (\nabla_y \mathbf{r})^T dy. \tag{A.2}$$

The tensor W and vector $\mathbf{r}$ are the solution of the following problems

$$\nabla_y^2 \mathsf{W}^T = \nabla_y \mathbf{m} - I \quad \text{in} \quad \Omega_v, \tag{A.3}$$

$$\nabla_y \cdot \mathsf{W}^T = 0 \quad \text{in} \quad \Omega_v, \tag{A.4}$$

$$\mathsf{W}^T \cdot \mathbf{n} = 0 \quad \text{on} \quad \Gamma, \tag{A.5}$$

$$\mathsf{W}^T \tau = -\bar{\varphi} [(\nabla_y \mathsf{W}^T) \mathbf{n}] \tau \quad \text{on} \quad \Gamma, \tag{A.6}$$

and

$$\nabla_y^2 \mathbf{r} = 0 \quad \text{in} \quad \Omega_t, \tag{A.7}$$

$$(\nabla_y \mathbf{r}) \cdot \mathbf{n}_t = \mathbf{n}_t \quad \text{on} \quad \Gamma, \tag{A.8}$$

respectively, where

$$\langle \mathbf{m} \rangle_v = 0 \quad \text{in} \quad \Omega_v, \quad \langle \mathbf{r} \rangle_t = 0 \quad \text{in} \quad \Omega_t. \tag{A.9}$$

The drug diffusivities F_v and F_t are given by

$$\mathsf{F}_v = \bar{D}_v (I - \langle (\nabla_y \mathbf{a})^T \rangle_v), \tag{A.10}$$

and

$$\mathsf{F}_t = \bar{D}_t (I - \langle (\nabla_y \mathbf{b})^T \rangle_t), \tag{A.11}$$

while the auxiliary fields $\mathbf{a}$ and $\mathbf{b}$ are the solution of the following microscale problems

$$\nabla_y^2 \mathbf{a} = 0 \quad \text{in} \quad \Omega_v, \tag{A.12}$$

$$(\nabla_y \mathbf{a}) \mathbf{n} = \mathbf{n} \quad \text{on} \quad \Gamma, \tag{A.13}$$

$$\nabla_y^2 \mathbf{b} = 0 \quad \text{in} \quad \Omega_t, \tag{A.14}$$

$$(\nabla_y \mathbf{b}) \mathbf{n} = \mathbf{n} \quad \text{on} \quad \Gamma. \tag{A.15}$$

The thermal conductivities N_v, and N_t are given by

$$\mathsf{N}_v = \bar{K}_v (I - \langle (\nabla_y \mathbf{g})^T \rangle_v), \tag{A.16}$$

$$\mathsf{N}_t = \bar{K}_t (I - \langle (\nabla_y \mathbf{e})^T \rangle_t), \tag{A.17}$$

where

$$\nabla_y^2 \mathbf{g} = 0 \quad \text{in} \quad \Omega_v, \tag{A.18}$$

$$(\nabla_y \mathbf{g}) \mathbf{n} = \mathbf{n} \quad \text{on} \quad \Gamma, \tag{A.19}$$

$$\nabla_y^2 \mathbf{e} = 0 \quad \text{in} \quad \Omega_t, \tag{A.20}$$

$$(\nabla_y \mathbf{e}) \mathbf{n} = \mathbf{n} \quad \text{on} \quad \Gamma. \tag{A.21}$$

In order for the solution of the cell problems related to the interstitial fluid flow, drug transport, and heat transport to be unique, a further condition is to be specified (for example by assuming the null cell average of the auxiliary variables in the cell), as shown by Cioranescu and Donato (1999) and Penta et al. (2015).

References

Abenojar, E.C., Wickramasinghe, S., Bas-Concepcion, J., Samia, A.C.S., 2016. Structural effects on the magnetic hyperthermia properties of iron oxide nanoparticles. Prog. Natl. Sci.: Mater. Int. 26 (5), 440–448.

Ademaj, A., Veltsista, D.P., Ghadjar, P., Marder, D., Oberacker, E., Ott, O.J., Wust, P., Puric, E., Hälg, R.A., Rogers, S., Bodis, S., Fietkau, R., Crezee, H., Riesterer, O., 2022. Clinical evidence for thermometric parameters to guide hyperthermia treatment. Cancers 14 (3), 625.

Al Sariri, T., Penta, R., 2022. Multi-scale modelling of nanoparticle delivery and heat transport in vascularised tumours. Math. Med. Biol. 39 (4), 332–367.

Avolio, M., Innocenti, C., Lascialfari, A., Mariani, M., Sangregorio, C., 2021. Medical applications of magnetic nanoparticles. In: New Trends in Nanoparticle Magnetism. Springer, pp. 327–351.

Bakhvalov, N., Panasenko, G., 1989. Homogenisation Averaging Processes in Periodic Media. Springer.

Bhuyan, B.K., Day, K.J., Edgerton, C.E., Ogunbase, O., 1977. Sensitivity of different cell lines and of different phases in the cell cycle to hyperthermia. Cancer Res. 37 (10), 3780–3784.

Bing, C., Patel, P., Staruch, R.M., Shaikh, S., Nofiele, J., Wodzak Staruch, M., Szczepan-ski, D., Williams, N.S., Laetsch, T., Chopra, R., 2019. Longer heating duration increases localized doxorubicin deposition and therapeutic index in Vx2 tumors using MR-HIFU mild hyperthermia and thermosensitive liposomal doxorubicin. Int. J. Hyperth. 36 (1), 195–202.

Boucher, Y., Brekken, C., Netti, P., Baxter, L., Jain, R., 1998. Intratumoral infusion of fluid: estimation of hydraulic conductivity and implications for the delivery of therapeutic agents. Br. J. Cancer 78 (11), 1442–1448.

Cervadoro, A., Giverso, C., Pande, R., Sarangi, S., Preziosi, L., Wosik, J., Brazdeikis, A., Decuzzi, P., 2013. Design maps for the hyperthermic treatment of tumors with superparamagnetic nanoparticles. PLoS One 8 (2), e57332.

Cherukuri, P., Glazer, E.S., Curley, S.A., 2010. Targeted hyperthermia using metal nanoparticles. Adv. Drug Deliv. Rev. 62 (3), 339–345.

Chicheł, A., Skowronek, J., Kubaszewska, M., Kanikowski, M., 2007. Hyperthermia–description of a method and a review of clinical applications. Rep. Pract. Oncol. Radiother. 12 (5), 267–275.

Cioranescu, D., Donato, P., 1999. An Introduction to Homogenization. Oxford University Press.

Colombo, M., Carregal-Romero, S., Casula, M.F., Gutierrez, L., Morales, M.P., Bohm, I.B., Heverhagen, J.T., Prosperi, D., Parak, W.J., 2012. Biological applications of magnetic nanoparticles. Chem. Soc. Rev. 41 (11), 4306.

Das, R., Alonso, J., Nemati Porshokouh, Z., Kalappattil, V., Torres, D., Phan, M.-H., Garaio, E., García, J.A., Sanchez Llamazares, J.L., Srikanth, H., 2016. Tunable high aspect ratio iron oxide nanorods for enhanced hyperthermia. J. Phys. Chem. C 120 (18), 10086–10093.

Das, P., Colombo, M., Prosperi, D., 2019. Recent advances in magnetic fluid hyperthermia for cancer therapy. Colloids Surfaces B 174, 42–55.

Decuzzi, P., Ferrari, M., 2006. The adhesive strength of non-spherical particles mediated by specific interactions. Biomaterials 27 (30), 5307–5314.

Dudar, T.E., Jain, R.K., 1984. Differential response of normal and tumor microcirculation to hyperthermia. Cancer Res. 44 (2), 605–612.

Famiani, S., LaGrow, A.P., Besenhard, M.O., Maenosono, S., Thanh, N.T.K., 2018. Synthesis of fine-tuning highly magnetic Fe@ Fe x O y nanoparticles through continuous injection and a study of magnetic hyperthermia. Chem. Mater. 30 (24), 8897–8904.

Ferguson, R.M., Khandhar, A.P., Jonasson, C., Blomgren, J., Johansson, C., Krish-nan, K.M., 2013. Size-dependent relaxation properties of monodisperse magnetite nanoparticles measured over seven decades of frequency by AC susceptometry. IEEE Trans. Magn. 49 (7), 3441–3444.

Gizzatov, A., Key, J., Aryal, S., Ananta, J., Cervadoro, A., Palange, A.L., Fasano, M., Stigliano, C., Zhong, M., Di Mascolo, D., et al., 2014. Hierarchically structured mag-netic nanoconstructs with enhanced relaxivity and cooperative tumor accumulation. Adv. Funct. Mater. 24 (29), 4584–4594.

Golneshan, A., Lahonian, M., 2011. The effect of magnetic nanoparticle dispersion on temperature distribution in a spherical tissue in magnetic fluid hyperthermia using the lattice Boltzmann method. Int. J. Hyperth. 27 (3), 266–274.

Gubin, S.P., 2009. Magnetic Nanoparticles. John Wiley & Sons.

Hergt, R., Dutz, S., Müller, R., Zeisberger, M., 2006. Magnetic particle hyperthermia: nanoparticle magnetism and materials development for cancer therapy. J. Phys.: Condens. Matter 18 (38), S2919.

Hilger, I., 2013. In vivo applications of magnetic nanoparticle hyperthermia. Int. J. Hyperth. 29 (8), 828–834.

Hornung, U., 1996. Homogenization and Porous Media, Vol. 6. Springer Science & Business Media.

Horsman, M.R., 2006. Tissue physiology and the response to heat. Int. J. Hyperth. 22 (3), 197–203.

Hossain, S.S., Zhang, Y., Liang, X., Hussain, F., Ferrari, M., Hughes, T.J., De-cuzzi, P., 2013. In silico vascular modeling for personalized nanoparticle delivery. Nanomedicine 8 (3), 343–357.

Jain, R.K., Baxter, L.T., 1988. Mechanisms of heterogeneous distribution of monoclonal antibodies and other macromolecules in tumors: significance of elevated interstitial pressure. Cancer Res. 48 (24 Part 1), 7022–7032.

Jain, R.K., Tong, R.T., Munn, L.L., 2007. Effect of vascular normalization by antian-giogenic therapy on interstitial hypertension, peritumor edema, and lymphatic metastasis: insights from a mathematical model. Cancer Res. 67 (6), 2729–2735.

Kappiyoor, R., Liangruksa, M., Ganguly, R., Puri, I.K., 2010. The effects of magnetic nanoparticle properties on magnetic fluid hyperthermia. J. Appl. Phys. 108 (9), 094702.

Kawai, N., Futakuchi, M., Yoshida, T., Ito, A., Sato, S., Naiki, T., Honda, H., Shirai, T., Kohri, K., 2008. Effect of heat therapy using magnetic nanoparticles conjugated with cationic liposomes on prostate tumor in bone. Prostate 68 (7), 784–792.

Kim, D.-H., Nikles, D.E., Johnson, D.T., Brazel, C.S., 2008. Heat generation of aqueously dispersed CoFe2O4 nanoparticles as heating agents for magnetically activated drug delivery and hyperthermia. J. Magn. Magn. Mater. 320 (19), 2390–2396.

Kok, H.P., Cressman, E.N.K., Ceelen, W., Brace, C.L., Ivkov, R., Grüll, H., ter Haar, G., Wust, P., Crezee, J., 2020. Heating technology for malignant tumors: a review. Int. J. Hyperth. 37 (1), 711–741.

Lang, J., Erdmann, B., Seebass, M., 1999. Impact of nonlinear heat transfer on temperature control in regional hyperthermia. IEEE Trans. Biomed. Eng. 46 (9), 1129–1138.

Laurent, S., Dutz, S., Häfeli, U.O., Mahmoudi, M., 2011. Magnetic fluid hyperthermia: focus on superparamagnetic iron oxide nanoparticles. Adv. Colloid Interface Sci. 166 (1–2), 8–23.

Law, M.P., 1979. Induced thermal resistance in the mouse ear: the relationship between heating time and temperature. Int. J. Radiat. Biol. Relat. Stud. Phys. Chem. Med. 35 (4), 481–485.

Less, J.R., Posner, M.C., Skalak, T.C., Wolmark, N., Jain, R.K., 1997. Geometric resistance and microvascular network architecture of human colorectal carcinoma. Microcirculation 4 (1), 25–33.

Mascheroni, P., Penta, R., 2017. The role of the microvascular network structure on diffusion and consumption of anticancer drugs. Int. J. Numer. Methods Biomed. Eng. 33 (10), e2857.

Miaskowski, A., Sawicki, B., 2013. Magnetic fluid hyperthermia modeling based on phantom measurements and realistic breast model. IEEE Trans. Biomed. Eng. 60 (7), 1806–1813.

Modok, S., Hyde, P., Mellor, H.R., Roose, T., Callaghan, R., 2006. Diffusivity and distribution of vinblastine in three-dimensional tumour tissue: Experimental and mathematical modelling. Eur. J. Cancer 42 (14), 2404–2413.

Muela, A., Munoz, D., Martin-Rodriguez, R., Orue, I., Garaio, E., Abad Diaz de Cerio, A., Alonso, J., García, J.A.n., Fdez-Gubieda, M.L., 2016. Optimal parameters for hyperthermia treatment using biomineralized magnetite nanoparticles: theoretical and experimental approach. J. Phys. Chem. C 120 (42), 24437–24448.

Nabil, M., Zunino, P., 2016. A computational study of cancer hyperthermia based on vascular magnetic nanoconstructs. R. Soc. Open Sci. 3 (9), 160287.

Ng, E.Y.K., Kumar, S.D., et al., 2017. Physical mechanism and modeling of heat generation and transfer in magnetic fluid hyperthermia through Néelian and Brownian relaxation: a review. Biomed. Eng. Online 16 (1), 1–22.

Oei, A.L., Vriend, L.E.M., Crezee, J., Franken, N.A.P., Krawczyk, P.M., 2015. Effects of hyperthermia on DNA repair pathways: one treatment to inhibit them all. Radiat. Oncol. 10 (1).

Overgaard, J., Radacic, M.M., Grau, C., 1991. Interaction of hyperthermia and cis-diamminedichloroplatinum (II) alone or combined with radiation in a C3H mammary carcinoma in vivo. Cancer Res. 51 (2), 707–711.

Pankhurst, Q.A., Connolly, J., Jones, S.K., Dobson, J., 2003. Applications of magnetic nanoparticles in biomedicine. J. Phys. D: Appl. Phys. 36 (13), R167.

Papanicolau, G., Bensoussan, A., Lions, J.-L., 1978. Asymptotic Analysis for Periodic Structures. Elsevier.

Penta, R., Ambrosi, D., 2015. The role of the microvascular tortuosity in tumor transport phenomena. J. Theoret. Biol. 364, 80–97.

Penta, R., Ambrosi, D., Quarteroni, A., 2015. Multiscale homogenization for fluid and drug transport in vascularized malignant tissues. Math. Models Methods Appl. Sci. 25 (01), 79–108.

Penta, R., Ambrosi, D., Shipley, R., 2014. Effective governing equations for poroelastic growing media. Q. J. Mech. Appl. Math. 67 (1), 69–91.

Penta, R., Merodio, J., 2017. Homogenized modeling for vascularized poroelastic materials. Meccanica 52 (14), 3321–3343.

Penta, R., Ramirez Torres, A., Merodio, J., Rodríguez-Ramos, R., 2021. Effective governing equations for heterogenous porous media subject to inhomogeneous body forces. Math. Eng. 3 (4), 1–17.

Perez, C.A., Sapareto, S.A., 1984. Thermal dose expression in clinical hyperthermia and correlation with tumor response/control. Cancer Res. 44 (10 Supplement), 4818s–4825s.

De la Presa, P., Luengo, Y., Multigner, M., Costo, R., Morales, M., Rivero, G., Hernando, A., 2012. Study of heating efficiency as a function of concentration, size, and applied field in γ-Fe2O3 nanoparticles. J. Phys. Chem. C 116 (48), 25602–25610.

Roohi, R., Baromand, S., Emdad, H., Mahmoudi, M.R., 2021. Optimization of focused multi-site injection therapy to provide the desired temperature pattern for arbitrary tumor configuration based on MNP hyperthermia: Implementation of dual phase lag bioheat equation. Ain Shams Eng. J. 12 (1), 901–915.

Roohi, R., Mahmoudi, M.R., Jafarpur, K., Emdad, H., 2020. Determination of Magnetic Nanoparticles Injection Characteristics for Optimal Hyperthermia Treatment of an Arbitrary Cancerous Cells Distribution. ASTM International.

Saeedi, M., Vahidi, O., Goodarzi, V., Saeb, M.R., Izadi, L., Mozafari, M., 2017. A new prospect in magnetic nanoparticle-based cancer therapy: Taking credit from mathematical tissue-mimicking phantom brain models. Nanomed.: Nanotechnol. Biol. Med. 13 (8), 2405–2414.

Sakaguchi, Y., Stephens, L.C., Makino, M., Kaneko, T., Strebel, F.R., Danhauser, L.L., Jenkins, G.N., Bull, J.M., 1995. Apoptosis in tumors and normal tissues induced by whole body hyperthermia in rats. Cancer Res. 55 (22), 5459–5464.

Salloum, M., Ma, R., Weeks, D., Zhu, L., 2008. Controlling nanoparticle delivery in magnetic nanoparticle hyperthermia for cancer treatment: experimental study in agarose gel. Int. J. Hyperth. 24 (4), 337–345.

Sarin, H., Kanevsky, A.S., Wu, H., Sousa, A.A., Wilson, C.M., Aronova, M.A., Griffiths, G.L., Leapman, R.D., Vo, H.Q., 2009. Physiologic upper limit of pore size in the blood-tumor barrier of malignant solid tumors. J. Transl. Med. 7 (1), 1–13.

Sawtarie, N., Cai, Y., Lapitsky, Y., 2017. Preparation of chitosan/tripolyphosphate nanoparticles with highly tunable size and low polydispersity. Colloids Surfaces B 157, 110–117.

Shipley, R.J., Chapman, S.J., 2010. Multiscale modelling of fluid and drug transport in vascular tumours. Bull. Math. Biol. 72 (6), 1464–1491.

Shubitidze, F., Kekalo, K., Stigliano, R., Baker, I., 2015. Magnetic nanoparticles with high specific absorption rate of electromagnetic energy at low field strength for hyperthermia therapy. J. Appl. Phys. 117 (9), 094302.

Stylianopoulos, T., Munn, L.L., Jain, R.K., 2018. Reengineering the physical microenvironment of tumors to improve drug delivery and efficacy: from mathematical modeling to bench to bedside. Trends Cancer 4 (4), 292–319.

Sweeney, P.W., d'Esposito, A., Walker-Samuel, S., Shipley, R.J., 2019. Modelling the transport of fluid through heterogeneous, whole tumours in silico. PLoS Comput. Biol. 15 (6), e1006751.

Tang, Y., 2018. Experimental investigation of applying MgCl2 and phosphates to synergistically inhibit the spontaneous combustion of coal. J. Energy Inst. 91 (5), 639–645.

Tang, Y.-d., Jin, T., Flesch, R.C., 2018. Impact of different infusion rates on mass diffusion and treatment temperature field during magnetic hyperthermia. Int. J. Heat Mass Transfer 124, 639–645.

Thomas, R., Park, I.-K., Jeong, Y.Y., 2013. Magnetic iron oxide nanoparticles for multimodal imaging and therapy of cancer. Int. J. Mol. Sci. 14 (8), 15910–15930.

Torres, T.E., Lima, E., Calatayud, M.P., Sanz, B., Ibarra, A., Fernández-Pacheco, R., Mayoral, A., Marquina, C., Ibarra, M.R., Goya, G.F., 2019. The relevance of Brownian relaxation as power absorption mechanism in Magnetic Hyperthermia. Sci. Rep. 9 (1), 1–11.